1987

# A Numerical Investigation of Low-Level Processes in Rapid Cyclogenesis

Nuss, Wendell A.; Anthes, Richard A.

American Meteorological Society

Nuss, Wendell A., and Richard A. Anthes. "A numerical investigation of low-level processes in rapid cyclogenesis." Monthly Weather Review 115.11 (1987): 2728-2743. https://hdl.handle.net/10945/62191

# A Numerical Investigation of Low-Level Processes in Rapid Cyclogenesis

WENDELL A. NUSS* AND RICHARD A. ANTHES

*National Center for Atmospheric Research,** Boulder, CO 80307*

(Manuscript received 22 October 1986; in final form 11 May 1987)

ABSTRACT

Several physical processes and properties of the initial state that affect marine cyclogenesis are examined using a mesoscale numerical model. The sensitivity of an idealized cyclone to the effects of latent heat release, surface heat and moisture fluxes as well as the initial meridional temperature gradient and static stability is examined by comparing various numerical stimulations of cyclogenesis in a baroclinic channel-flow model. Idealized initial conditions are derived analytically and are characterized by strong low-level baroclinity and a very weak upper-level trough. These initial conditions are used to examine which factors in baroclinic cyclogenesis are most important for rapid development (1 m $h^{-1}$ for 24 h or more) and how diabatic processes modify the development rate.

A strong low-level meridional temperature gradient (40°C/2000 km) and low static stability (a mean lapse rate of 6.0°C $km^{-1}$) resulted in rapid development of the model cyclone. The model cyclogenesis is more sensitive to small changes in the initial baroclinity than to physical processes during the development, which suggests that sustained rapid development requires substantial baroclinic instability. Inclusion of latent heat release during the development resulted in only a 10% increase in the average deepening rate. This effect of latent heating depended crucially upon the moisture distribution and is more representative of large-scale stable condensation than strong convection. Modification of the model cyclogenesis by various surface heat and moisture flux distributions indicated that the phase and magnitude of these fluxes relative to the low-level atmospheric baroclinity is important. A distribution of surface heating that enhanced the low-level baroclinity resulted in a 15% increase in the growth rate, suggesting an important interaction during certain periods of development. Surface heating distributions that reduced the low-level baroclinity by counteracting thermal advection damped the development of the model cyclone as suggested by previous studies.

## 1. Introduction

Explosively deepening cyclones in which central pressure deepening rates exceed 1 mb $h^{-1}$ for 24 h or more are described by Sanders and Gyakum (1980). Considerable controversy surrounds the relative importance of factors that contribute to rapid development. Roebber (1984) uses a statistical argument to suggest that explosive cyclogenesis is an unusual event that differs from typical baroclinic developments. Traditionally, baroclinic instability associated with the vertical shear of the jet stream is considered to be the primary mechanism that leads to atmospheric cyclogenesis. Rapid intensification of these explosive cyclones is explained by modification of baroclinic instability by various physical and dynamical processes. However, the relative roles of upper-level dynamical forcing, low-level baroclinity, latent heating, air–sea interaction and static stability to produce significantly larger deepening rates of marine cyclones are not known.

Upper-level dynamical forcing due to strong positive vorticity advection associated with a shortwave trough or jet streak and low-level forcing by strong low-level baroclinity are both known to influence cyclogenesis. Petterssen et al. (1962) and Petterssen and Smebye (1971) classified cyclogenesis into two types: type A, where the low-level baroclinity is the primary factor, and type B, where the influence of upper-level vorticity advection is the primary factor. The importance of upper-level forcing in contributing to explosive cyclogenesis is well documented. Sanders and Gyakum (1980) note in their climatology the correlation of explosive cyclogenesis and mobile 500 mb troughs. More recently, Sanders (1986) quantitatively established this relationship between upper-level vorticity advection and the explosive development of the surface cyclone with data from the 1981–84 cold seasons. For the explosively deepening Presidents' Day storm, Uccellini et al. (1984) found that processes associated with a propagating jet streak were significant in the rapid development. In addition, Bosart and Lin (1984) and Uccellini et al. (1985) found the influence of a tropopause fold to be important in producing the rapid development.

Other studies suggest that low-level baroclinity, latent heat release, heat and moisture fluxes from the ocean

* Present affiliation: Department of Meteorology, Naval Postgraduate School, Monterey, CA 93943.

** The National Center for Atmospheric Research is sponsored by the National Science Foundation.

or low static stability are the primary factors that contribute to explosive cyclogenesis. These studies suggest that upper-level forcing organizes the critical low-level contributions to result in rapid development. Gyakum (1983b) found that the latent heat release due to deep convection organized by baroclinic forcing in the *Queen Elizabeth II* (*QEII*) storm contributed significantly to the rapid cyclogenesis. In a numerical simulation study of a nonexplosive cyclone, Chen et al. (1983) show that upper-level forcing by an upstream trough provided the necessary structure to critical contributions by diabatic heating and boundary layer processes. Even for the Presidents' Day storm, Bosart (1981) and Bosart and Lin (1984) indicate that the low-level contributions by the surface heat and moisture fluxes were important to the cyclogenesis. Reed and Albright (1986) found that surface heat and moisture fluxes contributed to the development of low static stability and moist symmetric instability, which apparently enhanced the development of an eastern Pacific cyclone with only weak upper-level forcing. These studies suggest that the low-level environment and diabatic processes are crucial for explosive development under a variety of upper-level forcing conditions.

A channel-flow version of the Pennsylvania State University/National Center for Atmospheric Research (PSU/NCAR) mesoscale model is used to examine the relative role of low-level baroclinity, latent heat release, and surface heat and moisture fluxes in a baroclinically driven explosive cyclone. Previous studies such as Newton and Trevisan (1984), Buzzi et al. (1977) and others suggest that explosive cyclogenesis can be simulated in a baroclinic channel-flow model. However, these studies neglect diabatic processes that are considered important to atmospheric cyclogenesis. In this study, the more complete model physics of the PSU/NCAR model and analytically derived initial conditions are used in a series of numerical experiments to examine the relative influence of various physical processes on rapid cyclogenesis.

## 2. Cyclogenesis experiments

### *a. PSU/NCAR model description*

The PSU/NCAR mesoscale model was modified in several ways to perform the cyclogenesis simulations in this study. The basic model is described by Anthes and Warner (1978). Modifications of the basic model for this study include changing the lateral boundary conditions to run in channel-flow mode and including additional vertical levels. To run in channel-flow mode, the map scale factors in the equations of motion for the Lambert Conformal map projection are set to 1, the latitudinal variation of the Coriolis parameter is linear ($\beta$-plane), the east–west boundaries are periodic, and the north–south boundaries are constant in time. The horizontal domain of the model in these simulations is 4000 km × 4000 km with a 100 km grid spacing. The vertical structure is shown in Table 1. The full sigma levels are boundaries between 14 model layers. The 14 half-sigma levels correspond to the 14 layers and five of these layers are contained in the boundary layer. The model top is 100 mb. A full description of the horizontal and vertical grid structure, as well as the computational methods are found in Anthes and Warner (1978).

The version of the model used in this study includes the high-resolution planetary boundary layer (PBL) model described by Zhang and Anthes (1982). An important aspect of this PBL model is its inclusion of differing treatments of the stable and unstable PBL. The stable regime is based upon a first-order closure K-theory model in which the vertical diffusion coefficient depends upon the Richardson number. The unstable regime is characterized by a convective plume model in which the surface fluxes of heat and moisture are distributed throughout the PBL. The intensity of the vertical exchange through the PBL depends upon the stratification of the entire PBL and the magnitude of the surface fluxes. Consequently, the vertical stratification affects the momentum, temperature and moisture structure throughout the boundary layer.

Two aspects of cloud formation and precipitation are parameterized in the mesoscale model. Large-scale, nonconvective latent heat release that results from the condensation of water vapor when the relative humidity exceeds 100% is one aspect of the moisture cycle in the model. Excess moisture over saturation is removed and the latent heat is added to the thermodynamic equation by this nonconvective precipitation. The more difficult problem of convection in a conditionally unstable atmosphere is treated using a cumulus parameterization scheme described by Anthes (1977). This convective parameterization follows that of Kuo (1974)

TABLE 1. Model sigma levels, approximate corresponding pressure levels (mb), and initial data specification levels (mb) for the PSU/NCAR model simulations in this study. Initial boundary layer data are specified on sigma levels.

| Vertical index | Full $\sigma$ levels | Standard pressure (mb) | Half $\sigma$ levels (data levels) | Standard pressure (mb) |
|---|---|---|---|---|
| 1 | 1.0 | 1010 | 0.999 | 1009 |
| 2 | 0.998 | 1008 | 0.989 | 1000 |
| 3 | 0.98 | 992 | 0.970 | 983 |
| 4 | 0.96 | 974 | 0.945 | 960 |
| 5 | 0.93 | 946 | 0.913 | 931 |
| 6 | 0.895 | 914 | 0.864 | 886 |
| 7 | 0.833 | 858 | 0.803 | 831 |
| 8 | 0.772 | 803 | 0.723 | 758 |
| 9 | 0.679 | 718 | 0.618 | 662 |
| 10 | 0.556 | 606 | 0.494 | 550 |
| 11 | 0.432 | 493 | 0.371 | 438 |
| 12 | 0.309 | 381 | 0.247 | 325 |
| 13 | 0.185 | 268 | 0.123 | 212 |
| 14 | 0.06 | 155 | 0.03 | 127 |
| 15 | 0.0 | 100 | | |

which uses the total moisture convergence in a vertical column as the criteria to determine whether moist convection will result.

Cumulus convection is assumed to occur when the total moisture convergence exceeds 0.01 $gm^{-2}\ s^{-1}$ and the predicted cloud top exceeds 700 mb. A fraction $b$ of the condensed moisture goes into moistening the column and the remainder $(1 - b)$ goes into condensational heating. The heating and moistening rates as well as the functions that distribute them vertically are specified in a manner similar to Kuo and Anthes (1984). The vertical profiles of the convective heating and moisture distribution functions in this study give the maximum heating at about 600 mb, which is typical of midlatitude cyclones as suggested by the heat budget studies of Liou and Elsberry (1987) and Lin and Smith (1982).

### b. *Experimental design*

To test the influence of various factors on cyclogenesis, seven numerical model experiments are run starting from analytic initial conditions. These model simulations are designed to examine the influence of physical factors during the development of a baroclinically unstable cyclone and to determine the sensitivity of the cyclogenesis to several features of the initial state. The model cyclogenesis is sensitive to both the physical relationships specified in the initial conditions and the physical processes that are parameterized in the mesoscale model. Consequently, experiments are designed to examine both aspects of the simulated cyclogenesis.

The initial conditions in this study are based upon the hypothesis that baroclinic instability leads to the initial development of explosive cyclones, although other processes may contribute significantly during the rapid development of the cyclone. Three-dimensional temperature, height, wind and moisture distributions are specified that will yield moist baroclinic cyclogenesis. These fields are designed to be consistent with theoretical phase and structure relationships known for amplifying baroclinic waves, observational evidence from Rogers and Bosart's (1986) composite of explosive cyclones, and case studies. The basic set of initial conditions used in the control simulation produces an average deepening rate of around 1.4 mb $h^{-1}$ for the 27 h period between 9 and 36 h in the simulation.

Other experiments examine the modification of the intensification of the control model cyclone due to physical processes during development and the mean baroclinity and static stability of the initial state. These experiments are summarized in Table 2. Experiment 2 consists of insulating the atmosphere from the surface by setting the surface heat and moisture fluxes to zero throughout the simulation. Experiment 3 uses a different sea surface temperature distribution but retains complete model physics. Experiment 4 is a dry simulation so that all moist physics are not considered, but friction and sensible heating are included. Other experiments use initial conditions that are derived by modifying the control initial conditions. Experiments 5 and 6 have lower and higher mean static stabilities than the control and Exp. 7 uses a less intense mean meridional temperature gradient. All model simulations are for 48 h, with most of the development occurring between 12 and 36 h.

TABLE 2. Key physical factors and processes used in each of the seven model simulations. Only factors that differ from the control are noted.

| Experiment | Physics | $\gamma$ (°C $km^{-1}$) | $\Delta T_y$ (°C) | SST pattern |
|---|---|---|---|---|
| 1 (control) | complete | 6.0 | 40.0 | zonal |
| 2 (no fluxes) | no sfc. heat fluxes | 6.0 | 40.0 | zonal |
| 3 (wave SST) | complete | 6.0 | 40.0 | sinusoidal |
| 4 (no moisture) | no latent heat release | 6.0 | 40.0 | zonal |
| 5 (low stability) | complete | 6.5 | 40.0 | zonal |
| 6 (high stability) | complete | 5.0 | 40.0 | zonal |
| 7 (less $\nabla T$) | complete | 6.0 | 30.0 | zonal |

### c. *Initial conditions*

Initial conditions are generated analytically using a method similar to that described by Fritsch et al. (1980). The method consists of six steps:

1. Specification of a two-dimensional pressure distribution at a reference height of 5.5 km with the equation:

$$P = P_0 + \Delta P_x + \Delta P_y \tag{2.1}$$

where $\Delta P_x$ and $\Delta P_y$ are sinusoidal pressure perturbations and $P_0$ is a constant. The $\Delta P_x$ perturbation is determined from

$$\Delta P_x = a_x c_p(x) G_p(y) \sin\left[\frac{2\pi x}{L_x} + \Phi_2(y)\right], \tag{2.2}$$

where

$$c_p(x) = d_1\left[d_2 + \sin\left(\frac{2\pi x}{L_x}\right)\right] \tag{2.3}$$

introduces an east–west amplitude asymmetry between the trough and ridge, and

$$G_p(y) = \sin\left(\frac{\pi y}{L_y}\right) \tag{2.4}$$

forces the perturbation to vanish on the north and south boundaries. The $\Delta P_y$ perturbation is determined from

$$\Delta P_y = -a_{y_1} \tanh\left[\frac{y - y_c}{p_1 F_j(x) \cdot dy}\right] - a_{y_2} \tanh\left(\frac{y - y_c}{p_2 \cdot dy}\right), \tag{2.5}$$

where

$$F_j(x) = 1 - b \sin\left[\frac{2\pi x}{L_x} + \Phi_1(y)\right] \quad (2.6)$$

produces a jet streak in the flow by introducing different isobar packing along the flow. The constants $a_{y_1}$, $a_{y_2}$, $a_x$, $p_1$, $p_2$, $b$, $d_1$, $d_2$ and the phase functions $\Phi_1(y)$ and $\Phi_2(y)$ for the control initial conditions are listed in Table 3. The coordinates $x$, $y$ and $z$ are specified in km measured from the lower left corner of the model domain and $y_c$ is the center of the domain with $dy$ equal to the grid spacing of 100 km.

2. Specification of the three-dimensional temperature structure with the equation:

$$T(x, y, z) = T_0 + \gamma(z)\Delta z + \Delta T_x + \Delta T_y, \quad (2.7)$$

where $T_0$ is the surface temperature, $\gamma(z)$ is a vertically varying lapse rate, and $\Delta T_x$ and $\Delta T_y$ are sinusoidal functions which specify the two-dimensional structure. The $\Delta T_x$ perturbation is determined from

$$\Delta T_x = b_x D(z) c_T(x) G_T(y) \sin\left[\frac{2\pi x}{L_x} + \Phi_T(y, z)\right], \quad (2.8)$$

where

$$D(z) = \frac{1}{2} - \frac{1}{2}\tanh\left(\frac{z-7}{dz}\right) \quad (2.9)$$

$$\Phi_T(y, z) = \frac{\pi}{2}\left[\frac{z_0^2 - (z - z_0)^2}{z_0^2 - (z_R - z_0)^2}\right] + \Phi_2(y) \quad (2.10)$$

introduce vertical variation in the temperature wave amplitude and phase, where the reference level $z_R$ is 5.5 km, the level of maximum phase difference $z_0$ is 7 km and $dz$ is a vertical grid spacing of 1 km. And,

$$c_T(x) = d_{t_1}\left[d_{t_2} + \sin\left(\frac{2\pi x}{L_x}\right)\right] \quad (2.11)$$

$$G_T(y) = \sin\left(\frac{\pi y}{L_y}\right) \quad (2.12)$$

are similar to the corresponding functions (2.3 and 2.4) in the pressure wave. The $\Delta T_y$ perturbation is determined from:

$$\Delta T_y = -b_{y_1}\tanh\left(\frac{y - y_c}{p_{b_1} \cdot dy}\right) - b_{y_2}\tanh\left(\frac{y - y_c}{p_{b_2} \cdot dy}\right) + F_R(x, y, z), \quad (2.13)$$

where

$$F_R(x, y, z) = f(z)\left[\sin\left(\frac{2\pi x}{L_x} + \pi\right) + \sin\left(\frac{2\pi y}{L_y}\right)\right]\sin^2\left(\frac{\pi x}{L_x}\right)\sin^2\left(\frac{\pi y}{L_y}\right) \quad (2.14)$$

$$f(z) = a_f\left[\frac{1}{2} - \frac{1}{2}\tanh\left(\frac{2z-3}{dz}\right)\right] \quad (2.15)$$

produces a more intense low-level temperature gradient or front near the surface that decreases with height according to the function $f(z)$. The constants $y_c$, $dy$ and $dz$ are the same as those used in (2.5) and (2.9). The other constants $T_0$, $b_{y_1}$, $b_{y_2}$, $b_x$, $a_f$, $p_{b_1}$, $p_{b_2}$, $d_{t_1}$, $d_{t_2}$ and the phase function $\Phi_2(y)$ for the control initial conditions are listed in Table 4. The vertical temperature variation $\gamma(z)\Delta z$ is specified from the parabolic function:

$$\gamma(z)\Delta z = (4hk)^{1/2} - [4h(z + k)]^{1/2}, \quad (2.16)$$

where the constants $k$ and $h$ are determined from

$$h = s^2 k \quad (2.17)$$

$$k = \frac{\left(\frac{\Delta T}{2s}\right)^2}{z_0 - 2\left(\frac{\Delta T}{2s}\right)}, \quad (2.18)$$

where the lapse rate at the surface $s$ is 6.5° km$^{-1}$ and the mean surface to 10 km temperature difference $\Delta T$ is 60°C for the control initial conditions.

3. Specification of the three-dimensional moisture structure by equations for the relative humidity similar to those used for the temperature. The relative humidity is then converted to mixing ratio.

4. Hydrostatic integration to determine the pressure distribution at all height levels and interpolation of the

TABLE 3. Constants used to specify the reference level pressure distribution for the control initial conditions.

| Reference pressure wave constants | |
|---|---|
| *Reference level pressure* | |
| $P_0$ | 462 mb |
| *Wavelength* | |
| $L_x$, $L_y$ | 4000 km |
| *Amplitude factors* (mb) | |
| $a_{y_1}$ | 10 |
| $a_{y_2}$ | 18 |
| $a_x$ | 3 |
| *Packing and structure* | |
| $p_1$ | 9 |
| $p_2$ | 12 |
| $b$ | 0.0 |
| $d_1$ | ¼ |
| $d_2$ | 3.0 |
| $f$ | 1.0 |
| *Phase relations* | |
| $\phi_1(y)$ | $\phi_2(y) - 5\pi/8 = 3\pi/8$ |
| $\phi_2(y)$ | $\pi$ |

TABLE 4. Constants used to specify the three-dimensional temperature distribution for the control initial conditions.

| Temperature wave constants | |
|---|---|
| *Reference level temperature* | |
| $T_0$ | 278 K |
| *Wavelength* | |
| $L_x, L_y$ | 4000 km |
| *Amplitude factors* (°C) | |
| $b_{y_1}$ | 12 |
| $b_{y_2}$ | 7 |
| $b_z$ | 5 |
| $a_f$ | 1 |
| *Packing and structure* | |
| $p_{b_1}$ | 11 |
| $p_{b_2}$ | 8 |
| $d_{t_1}$ | ¼ |
| $d_{t_2}$ | 3.0 |
| $d$ | 1.0 |
| *Phase relations* | |
| $\phi_2(y)$ | $\pi$ |

pressure distribution on height levels to height distributions on pressure levels.

5. Determination of the winds from the nonlinear balance equation in pressure coordinates:

$$\nabla^2\phi - f\zeta + (\mathbf{k}\times\mathbf{V})\cdot\nabla f - 2J(u,v) = 0 \quad (2.19)$$

above the PBL and the model of Brown and Liu (1982) within the PBL.

6. Interpolation of initial fields on pressure levels to the 14 model sigma levels.

The choices for sinusoidal or other mathematical functions and constants used in the equations are arbitrary. However, factors such as the mean meridional temperature gradient, vertical lapse rate or static stability, the phase between the 500 mb geopotential wave and three-dimensional temperature structure, and the resultant surface pressure distribution serve as adjustable factors to produce realistic pre-cyclogenetic structure. Nuss (1986) provides a more complete description.

The wind and thermal structures in the initial conditions for the control experiment are highly favorable for baroclinic instability. The meridional cross section of temperature and zonal wind along the western boundary of the channel is shown in Fig. 1 and indicates the highly baroclinic structure of the model atmosphere. The horizontal temperature gradient is concentrated into a 1500 km baroclinic zone, which produces a 60 m $s^{-1}$ jet stream core at the tropopause level. The vertical wind shear and meridional temperature gradient are both larger than the mean wintertime conditions for the eastern North America sector in Lau (1978) and the composite polar low genesis cross section in Mullen (1979). However, the vertical wind shear and horizontal temperature gradient are representative of the composite explosive cyclone conditions in Rogers and Bosart (1986).

To release the baroclinic instability of the environmental flow, traditional channel-flow baroclinic instability studies introduce small perturbations into the basic flow. This study differs from other channel-flow studies by using initial conditions that attempt to replicate realistic atmospheric conditions during the early stages of oceanic cyclogenesis. The 500 mb geopotential height and temperature distributions are shown in Fig. 2. The amplitude of the 500 mb geopotential wave is small, which results in only small positive vorticity advection, similar to the Petterssen and Smeybe (1971) type A cyclogenesis conditions. The larger amplitude of the temperature wave results in substantial warm and cold advection at 500 mb and throughout the lower troposphere, as indicated by the surface pressure, temperature and wind analysis shown in Fig. 3. Thickness advection is therefore favorable for strong vertical motions and intensification of this baroclinic wave. In addition, the prescribed temperature wave lags the 500 mb geopotential wave by approximately ¼ wavelength (900 km) and results in a thermal structure that is energetically favorable for intensification. Although the large surface perturbation and weak upper-level wave may not be typical, case studies such as Reed and Albright (1986) indicate that this situation is found in the atmosphere.

The static stability is another important factor in prescribing the initial conditions. The mean lapse rate or static stability for the initial state shown in Fig. 1 is

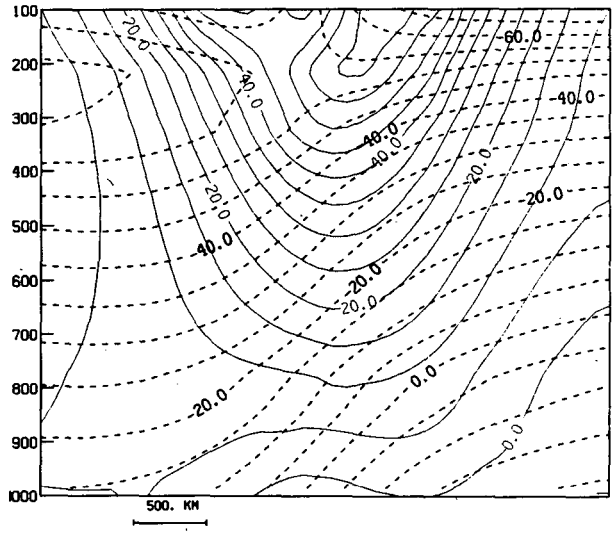


FIG. 1. Vertical cross section of the initial wind speed (solid) and temperature (dashed) along the western boundary for the control simulation. Wind is in m $s^{-1}$ with a 5 m $s^{-1}$ contour interval. Temperature is in °C with a 5°C contour interval. Horizontal length scale in km appears at the bottom.

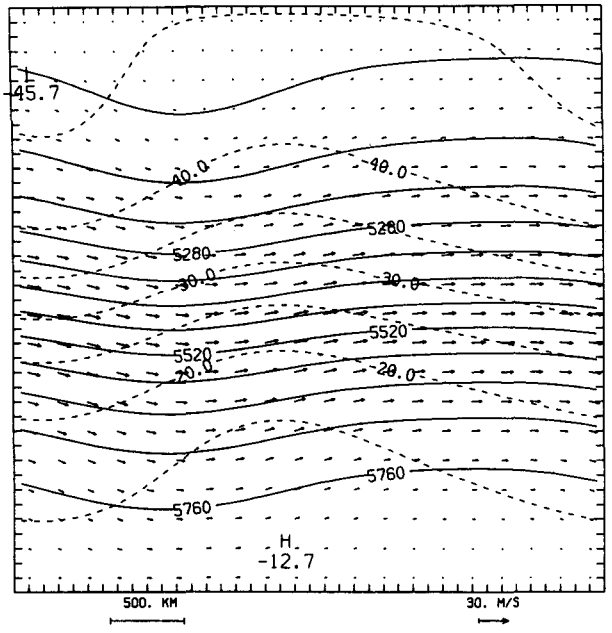


FIG. 2. Initial 500 mb geopotential height (solid), air temperature (dashed) and wind vectors for the control simulation. Geopotential height is in m with a 60 m contour interval. Temperature is in °C with a 5°C contour interval. Wind vectors vary in length according to speed: 30 m $s^{-1}$ wind vector scale given at the bottom. Horizontal length scale in km appears at the bottom.

6.0° $km^{-1}$, similar to the mean wintertime conditions of Lau (1978) and to the composite lapse rate in Rogers and Bosart (1986). However, the static stability in the model is slightly lower near the surface due to the parabolic vertical temperature structure. Horizontal variation within the cyclone is such that the warm sector is more unstable than the cold sector as illustrated by the representative soundings in Fig. 4. The warm sector sounding is moist and is associated with a lifted index of −8, which indicates large potential instability. The cold sector is more stable and much drier than the warm sector, which is typical of the subsidence region of a cyclone.

Although the above factors provide sufficient conditions for baroclinic instability, the heat and moisture fluxes from the surface are potentially important effects, and thus the sea surface temperature (SST) must also be specified. The zonally oriented SST distribution shown in Fig. 5 for the control simulation is oriented to reinforce the mean baroclinity in the atmosphere. Climatological values of the temperature gradient and overall change from warm to cold water for the Gulf Stream off the east coast of the U.S. are approximately 3°C/100 km and 20°C, similar to those in Fig. 5. The associated total surface heat flux (latent plus sensible) at the initial time is also shown in Fig. 5. This pattern is similar to that found by Petterssen et al. (1962) for incipient wave cyclones. This pattern of surface heating introduces temperature tendencies that counteract the initial thermal advection.

The control initial conditions are used in Exps. 2 and 4 as well as Exp. 1. Modifications to these control initial conditions are made for some of the experiments listed in Table 2. To test the influence of the different SST distribution in Exp. 3, a sinusoidal SST structure replaced the zonal SST distribution used in the control simulation and is shown in Fig. 6. The sinusoidal SST distribution reinforces the low-level baroclinity instead of the large-scale mean baroclinity. The initial surface fluxes associated with this SST distribution are also shown in Fig. 6.

To test the influence of static stability, the mean surface to 10 km lapse rates are increased to 6.5° $km^{-1}$ in Exp. 5 and decreased to 5.0° $km^{-1}$ in Exp. 6, respectively. The lapse rate near the surface increased to 7.5° $km^{-1}$ in Exp. 5 and decreased to 6.0 $km^{-1}$ in Exp. 6 compared to 6.5° $km^{-1}$ for the control experiment. Other factors in the initial conditions are left unchanged.

To test the effect of baroclinity, the mean meridional temperature difference is reduced from 40°C to 30°C in Exp. 7 to produce a less baroclinic initial state. Other factors are similar to the control conditions with some shortening of the thermal wavelength to yield a closed circulation at the surface, similar to the other initial states.

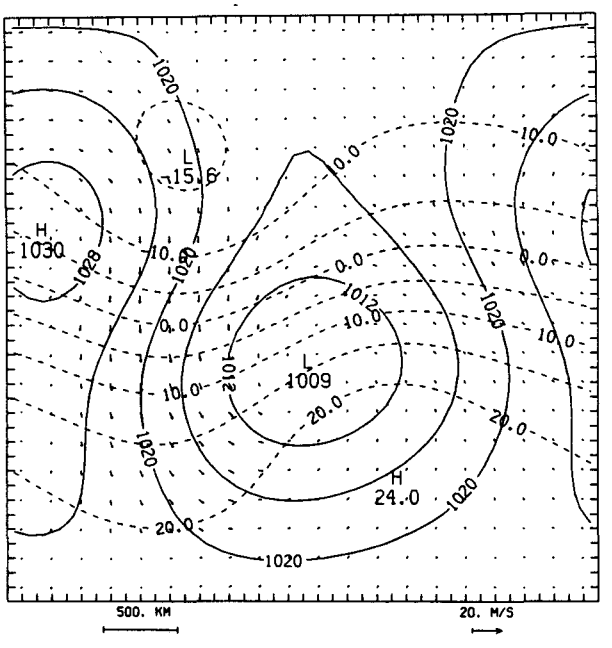


FIG. 3. Initial sea level pressure (solid), surface air temperature (dashed) and surface wind vectors for the control simulation. Pressure is in mb with a 4 mb contour interval. Temperature is in °C with a 5°C contour interval. Wind vectors vary in length according to speed: 20 m $s^{-1}$ wind vector scale given at the bottom. Horizontal length scale in km appears at the bottom.

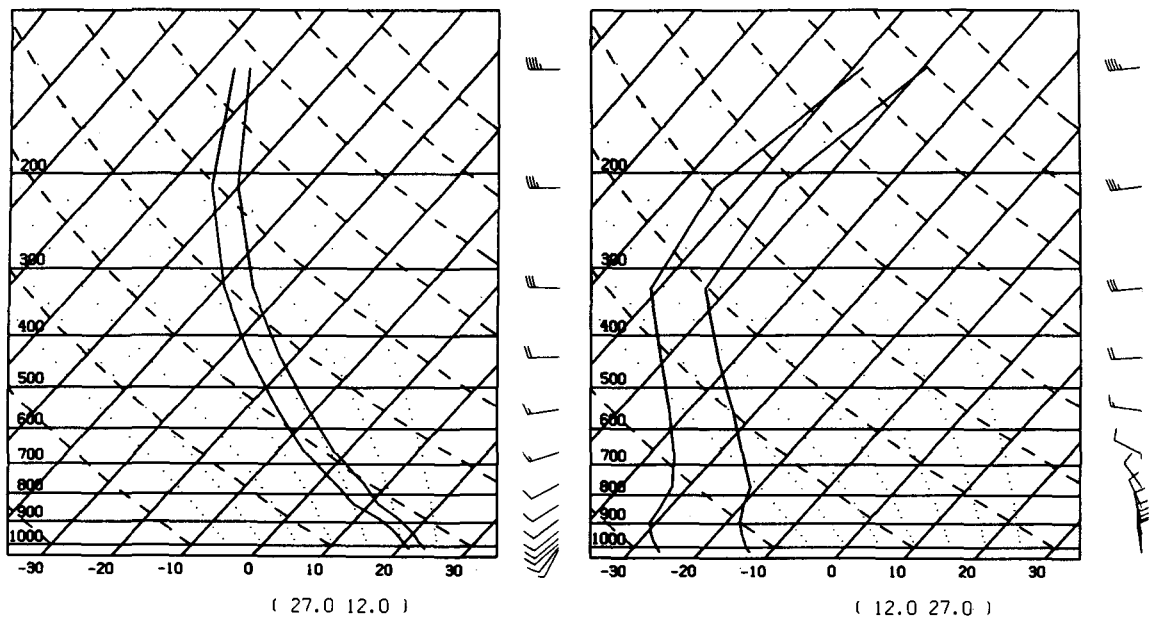


FIG. 4. Initial warm sector (a) and cold sector (b) temperature (right) and dewpoint (left) soundings for the control simulation on a skew $T$–log$P$ chart. Dry adiabats are dashed, moist adiabats are dotted, temperature lines are sloping solid (bottom labels) and pressure lines are horizontal solid (left labels in mb). Wind vectors are in m s$^{-1}$ with each full barb equal to 10 m s$^{-1}$. Grid point location appears at the bottom.

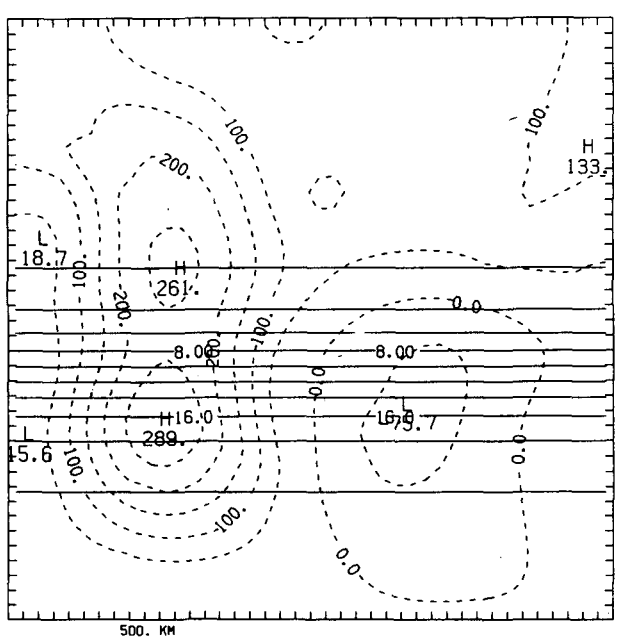


FIG. 5. Sea surface temperature (solid) and initial total (latent plus sensible) surface heat flux (dashed) distributions for the control simulation. Temperature is in °C with a 2°C contour interval. Heat flux is in W m$^{-2}$ with a 50 W m$^{-2}$ contour interval. Negative values indicate a downward flux. Horizontal length scale in km appears at the bottom.

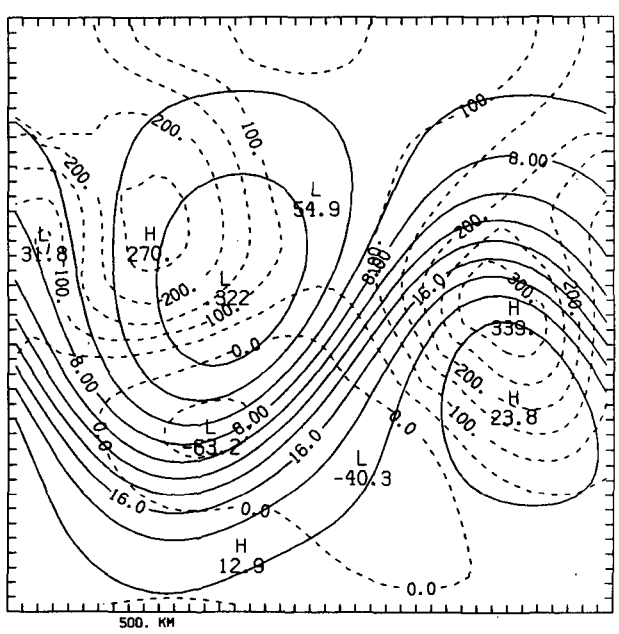


FIG. 6. As in Fig. 5 except for the sinusoidal SST simulation.

## 3. Results

### *a. Development of the model cyclone*

By the Sanders and Gyakum (1980) definition of explosive development ( 1 mb $h^{-1}$ for 24 h or more), the model cyclone develops explosively, as demonstrated by the time series of central pressure for the experiments shown in Fig. 7. The development increases when the fluxes are removed (Exp. 2), the SST distribution is in phase (Exp. 3) or the static stability is reduced (Exp. 5) and the development decreases when there is no latent heating (Exp. 4), higher static stability (Exp. 6) or a smaller meridional temperature gradient (Exp. 7). The development of the model cyclone in all experiments is characterized by a 27 h period of steady deepening between 9 h and 36 h with an average rate of 1.46 mb $h^{-1}$ for the control experiment. This rate is three times the estimated quasi-geostrophic rate computed from the model data at 12 h using the model of Sanders (1971), which indicates the importance of diabatic and nonlinear processes in the model cyclone.

The structure of the model cyclone after 24 h of simulation provides a representative view of the cyclogenesis during the period of most rapid development. The initial 1009 mb low has intensified significantly and deepened to a 986 mb low as shown in Fig. 8. Cold and warm fronts are indicated by the wind and pressure fields in Fig. 8 and confirmed by the surface relative vorticity distribution shown in Fig. 9. The maximum cyclonic vorticity at the surface has increased from 2.7 $\times 10^{-5}$ $s^{-1}$ at the initial time to 10.7 $\times 10^{-5}$ $s^{-1}$ at 24 h (Fig. 9). Intense surface heat and moisture fluxes (Fig. 10) strongly modify the boundary layer temperature structure (Fig. 8) and prevent the formation of concentrated surface temperature gradients and strong

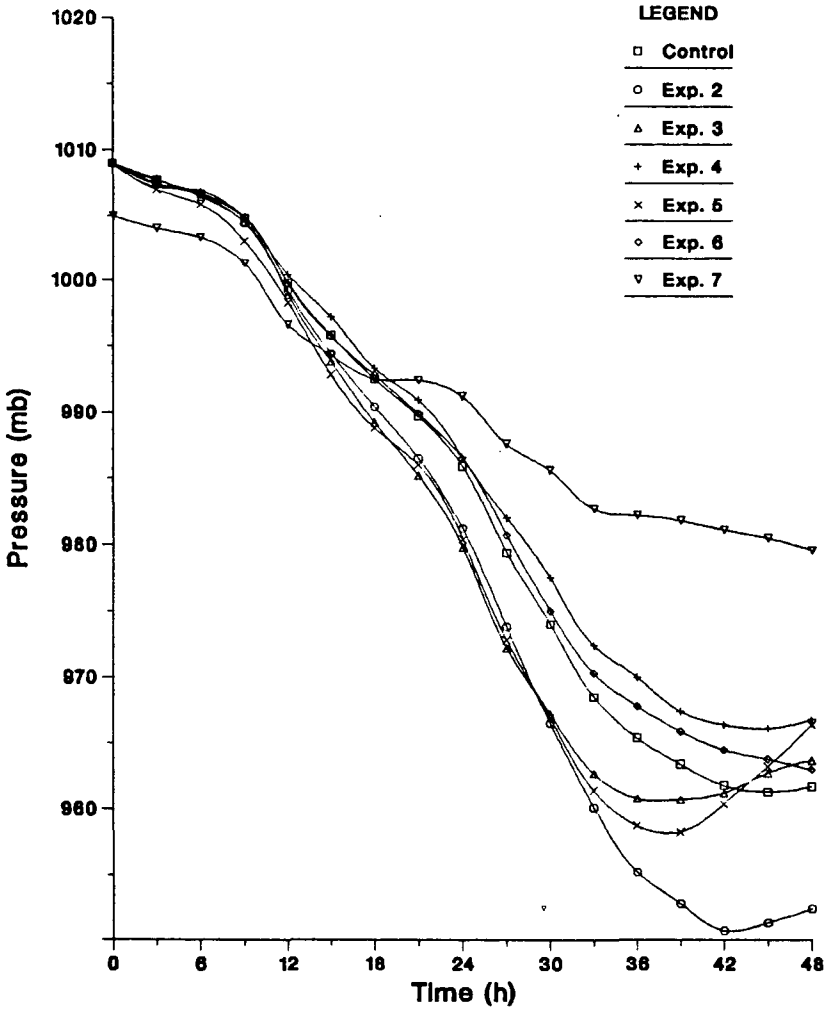


FIG. 7. Time series of central sea level pressure in mb for the seven model experiments. Lines labeled with the experiment numbers given in Table 2 and described in text.

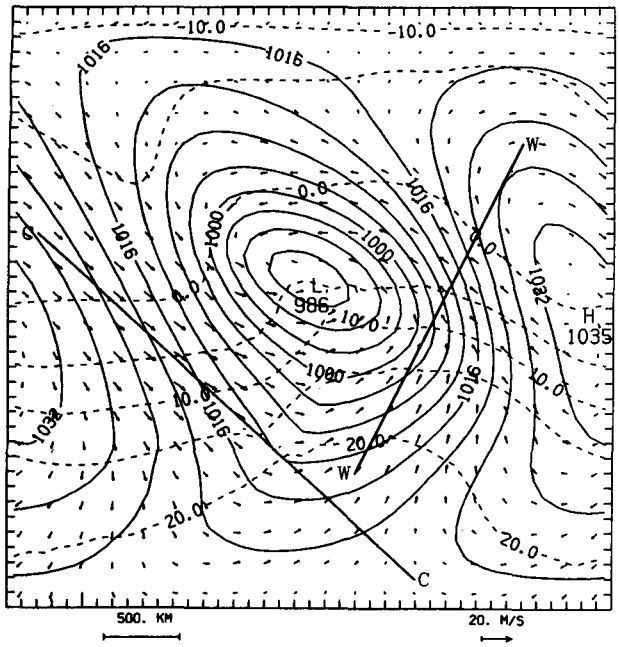


FIG. 8. Sea level pressure (solid), surface air temperature (dashed) and surface wind vectors for the control simulation at 24 h. Contours and labels as in Fig. 3. Cross sections constructed along lines C–C (Fig. 13a) and W–W (Fig. 13b).

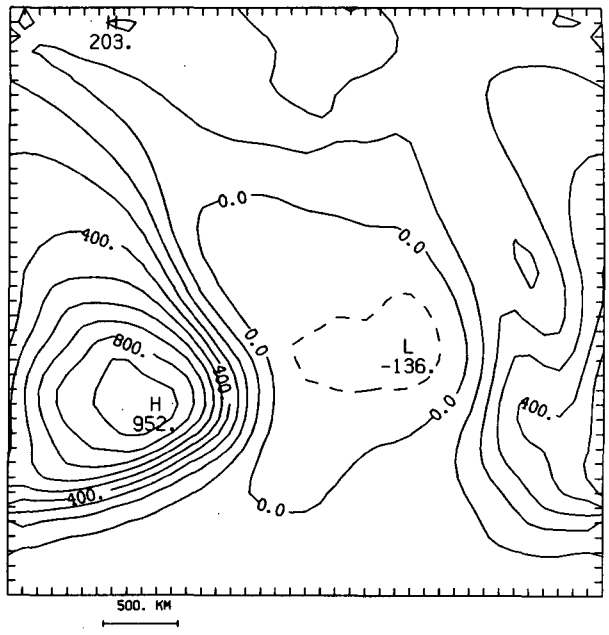


FIG. 10. Total surface heat flux (latent plus sensible) at 24 h for the control simulation. Heat flux is in W $m^{-2}$ with a 100 W $m^{-2}$ contour interval. Negative values indicate a downward flux.

temperature advection associated with these fronts. The effect of the strong air–sea interaction extends only to the top of the boundary layer, as suggested by the stronger temperature gradient and temperature advection at 850 mb (Fig. 11). At upper levels the geopotential height wave has amplified considerably during the

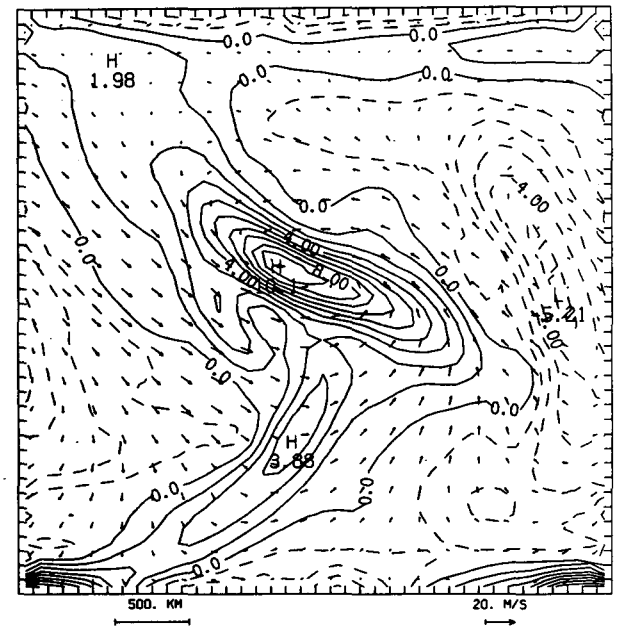


FIG. 9. Surface relative vorticity and wind vectors for the control simulation at 24 h. Relative vorticity is in $10^{-5}$ $s^{-1}$ with a $1 \times 10^{-5}$ $s^{-1}$ contour interval. Positive values are cyclonic vorticity. Wind vectors as in Fig. 3.

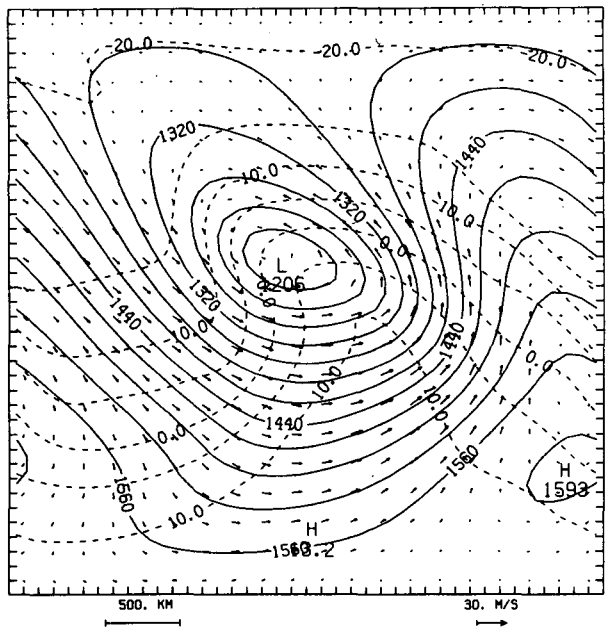


FIG. 11. 850 mb geopotential height (solid), temperature (dashed) and wind vectors for the control simulation at 24 h. Geopotential height is in m with a 30 m contour interval. Temperature is in °C with a 5°C contour interval. Wind vectors vary in length according to speed: 30 m $s^{-1}$ wind vector scale given at the bottom.

24 h and is shown in Fig. 12. The maximum relative vorticity in the 500 mb trough has increased to $9 \times 10^{-5}$ $s^{-1}$ in Fig. 12 compared to the initial $3 \times 10^{-5}$ $s^{-1}$, which was primarily shear vorticity. As a result, the cyclonic vorticity advection over the surface cyclone has increased.

Two important aspects of the moisture and vertical circulation are revealed in the cross section through the cold front (line C–C in Fig. 8) shown in Fig. 13a. Large surface heat and moisture fluxes produce significant boundary layer mixing and a layer of saturation resembling stratocumulus clouds in the cold air, which is typical of oceanic cyclones. Estimated PBL height and cloud depths are similar to those found by Agee and Lomax (1978) for mesoscale cellular convection during the Air Mass Transformation Experiment (AMTEX). The latent heating in the shallow stratocumulus clouds and the surface sensible heat flux counteract the cold advection in the boundary layer west of the surface low. In addition to the high boundary layer moisture, a deep, moist band is observed along the cold front (Fig. 13a) which indicates a significant cold frontal vertical circulation. For the warm front region (line W–W in Fig. 8), a much broader area of high relative humidity is found (Fig. 13b), which suggests a broad region of ascent and latent heat release in the warm sector of the cyclone. The cloud distribution implied by the relative humidity structure and the inferred vertical circulation shown in these cross sections is typical of marine cyclones.

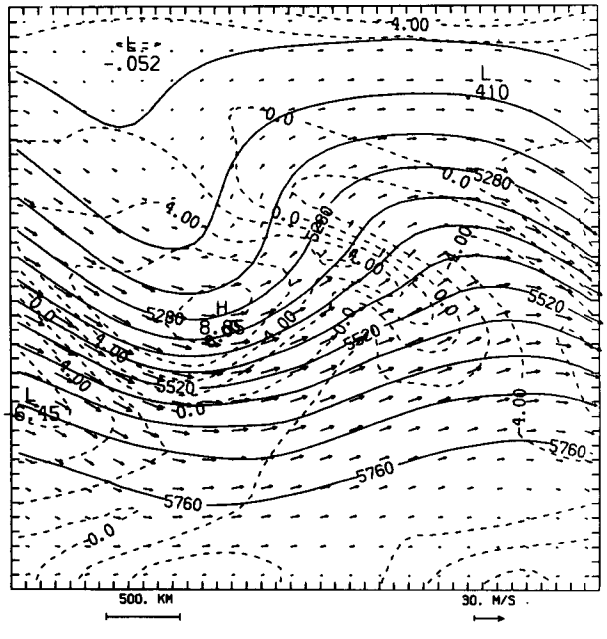


FIG. 12. 500 mb geopotential height (solid), relative vorticity (dashed) and wind vectors for the control simulation at 24 h. Relative vorticity is in $10^{-5}$ $s^{-1}$ with a $2 \times 10^{-5}$ $s^{-1}$ contour interval. Positive values are cyclonic vorticity. Wind vectors and geopotential contours as in Fig. 2.

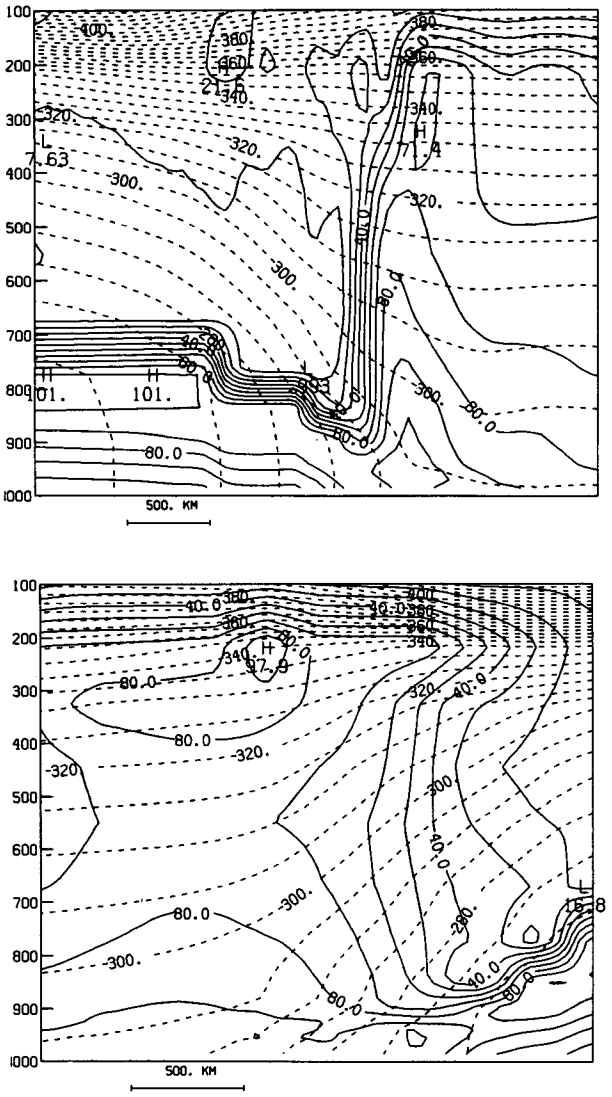


FIG. 13. Cross section of potential temperature (dashed) and relative humidity (solid) through (a) cold front along line C–C in Fig. 8 and (b) warm front along line W–W in Fig. 8 for the control simulation at 24 h. Potential temperature is in °C with a 5° contour interval. Relative humidity is in % with a 10% contour interval. Vertical coordinate is pressure in mb. Horizontal length scale in km appears at the bottom.

The upper-level wave amplification and the surfce cyclogenesis can be interpreted from the perspective of baroclinic self-development as first described by Sutcliffe and Forsdyke (1950). Initially, substantial warm advection and diabatic heating along the warm front act to increase the amplitude of the upper-level wave. In response to this amplification, the 500 mb vorticity advection increases, which through the induced vertical circulation leads to boundary layer convergence that amplifies the vorticity of the surface cyclone. Heat and vorticity budgets analyzed for the model cyclone confirm that significant thermal advection develops prior

to increased vorticity advection. In addition, the budgets show that significant upper-level divergence and an associated vertical circulation develop within 6 h in response to the baroclinically unstable initial conditions.

Significant amplification at both upper and lower levels occurs in the next 12 h to produce a substantially more intense surface cyclone at 36 h as shown in Fig. 14. The boundary layer thermal structure is similar to that found at 24 h and indicates strong modification by the surface heat fluxes. The maximum cyclonic vorticity at the surface had increased to $14 \times 10^{-5}$ s$^{-1}$ and the frontal vorticity is essentially unchanged indicating no intensification of the front. The 500 mb wave and vorticity have increased as shown in Fig. 15. The 500 mb vorticity increased more during this 12 h period than did the surface vorticity, a result consistent with the interpretation that the low-level thermal advection and diabatic processes are driving the upper-level amplification. In response to the amplification at upper levels, upper-level frontogenesis and tropopause folding occur in the region upstream from the 500 mb trough as revealed in the cross section (line P–P in Fig. 15) of potential vorticity and potential temperature shown in Fig. 16. This upper-level frontogenesis has previously been investigated in a channel-flow model of baroclinic instability by Newton and Trevisan (1984).

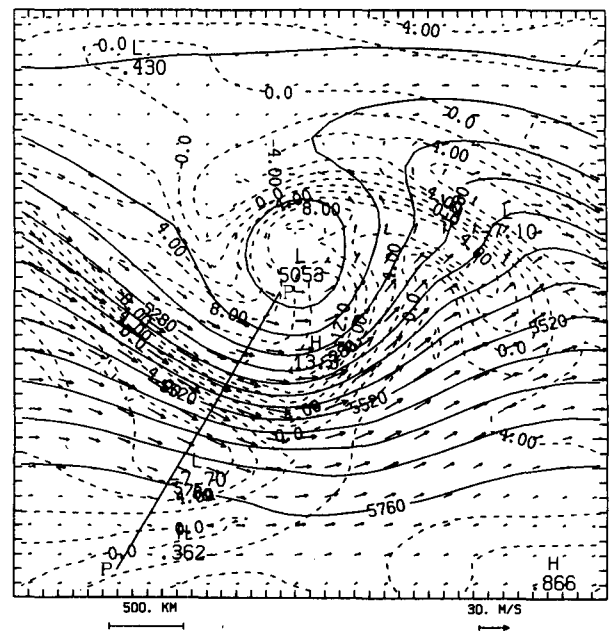


FIG. 15. 500 mb geopotential height (solid), relative vorticity (dashed) and wind vectors for the control simulation at 36 h. Contours and labels as in Fig. 12. Cross section constructed along line P–P (Fig. 16).

*b. Physical influences during development*

As shown in Fig. 7, the removal of the surface heat and moisture fluxes in Exp. 2 increases the surface cyclogenesis rate. Without surface heat and moisture fluxes, the average deepening rate over 27 h increased by 25% to 1.82 mb h$^{-1}$ and a more intense surface cyclone develops. The surface pressure, temperature

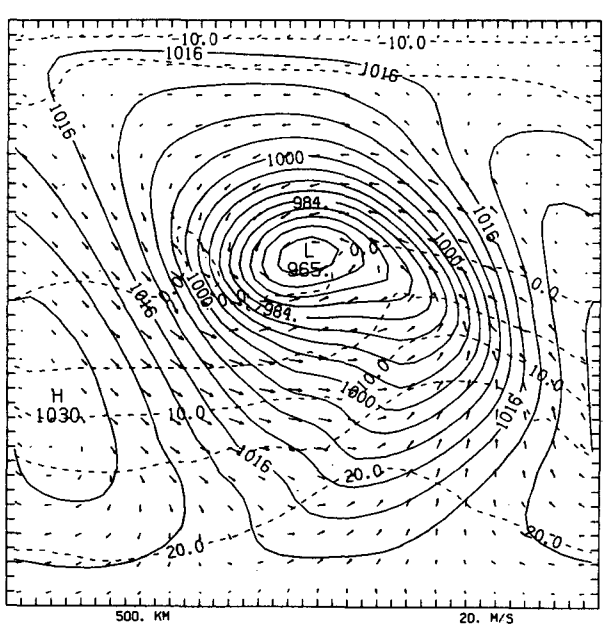


FIG. 14. Sea level pressure (solid), surface air temperature (dashed) and surface wind vectors for the control simulation at 36 h. Contours and labels as in Fig. 3.

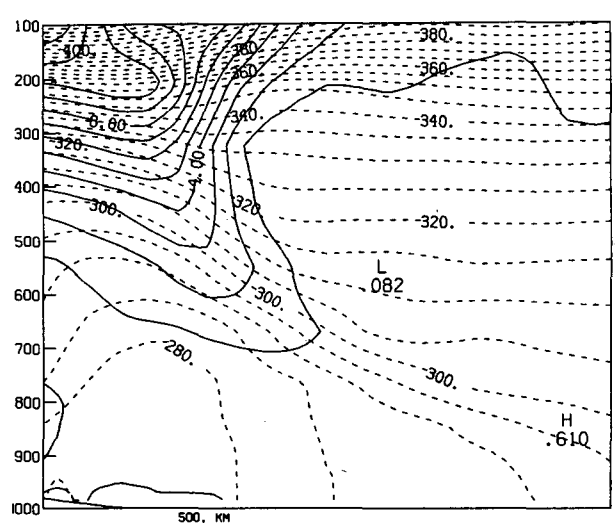


FIG. 16. Cross section along line P–P (Fig. 15) of potential vorticity (solid) and potential temperature (dashed) for the control simulation at 36 h. Potential vorticity is in $10^{-5}$ K s$^{-1}$ mb$^{-1}$ with a $1 \times 10^{-5}$ K s$^{-1}$ mb$^{-1}$ contour interval. Potential temperature is in °C with a 5° contour interval. Vertical coordinate is pressure in mb. Horizontal length scale in km given at the bottom.

and wind distributions at 24 h are shown in Fig. 17. The primary differences from the control are that the low-level thermal advection has increased and the temperature gradients along both the warm and cold fronts are stronger (compare with Fig. 8). Associated with this modification of the boundary layer temperatures are an increase in the boundary layer static stability in the cold air west of the cyclone center and a decrease east of the cyclone center in the warm sector. The surface temperature difference between the control and Exp. 2 are shown in Fig. 18; they correspond closely to the total heat flux distribution at 24 h in the control simulation (Fig. 10). At 24 h, the central pressure difference is relatively small. However, by 36 h this difference has magnified substantially as shown by comparing Figs. 19 and 14. At 500 mb, the geopotential height wave amplitude is greater than in the control and there is a general lowering of the heights. However, nearly identical height decreases occur at 850 mb, which results in a similar 500–850 mb thickness distribution in both the control and Exp. 2. Consequently, the differential vorticity advection is similar in both experiments, which suggests that the upper-level dynamical forcing is essentially unchanged. The vertical velocity at 850 mb is nearly equal in Exp. 2 and the control, which confirms that the dynamical forcing is similar.

Experiment 3, which uses the sinusoidal SST distribution shown in Fig. 6, also develops more rapidly and indicates that damping by the surface heating is reduced or reversed when the distribution of SST is in phase with the PBL temperature structure. The surface pressure, temperature and wind distributions at 24 h for a simulation using the sinusoidal SST distribution is

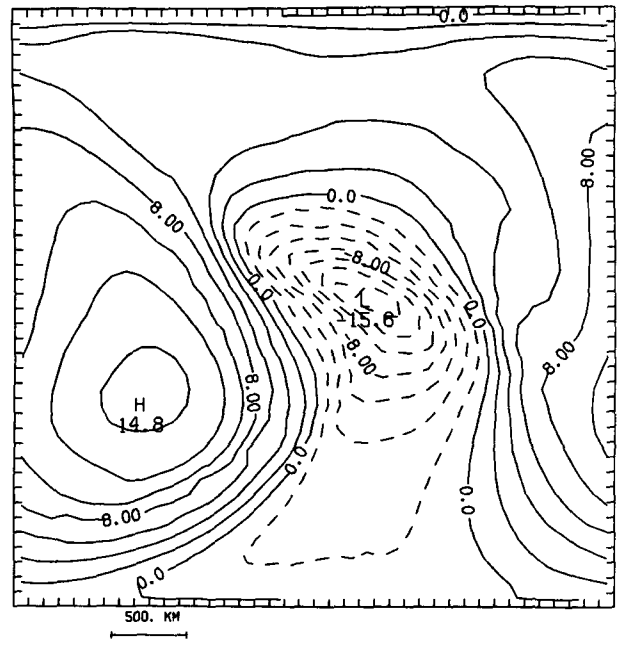


FIG. 18. Air temperature difference at the surface between the control simulation and the no heat flux simulation. Temperature is in °C with a 2°C contour interval. Positive values indicate that control simulation has higher surface temperature.

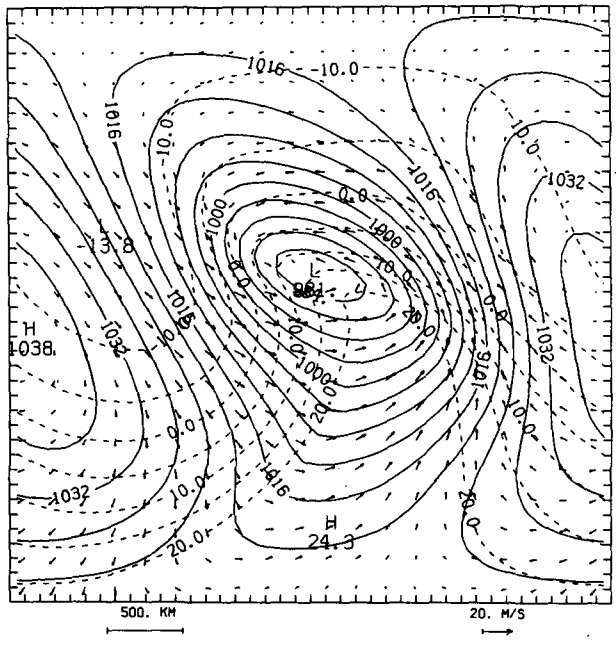


FIG. 17. Sea level pressure (solid), surface air temperature (dashed) and surface wind vectors for the no heat flux simulation at 24 h. Contours and labels as in Fig. 3.

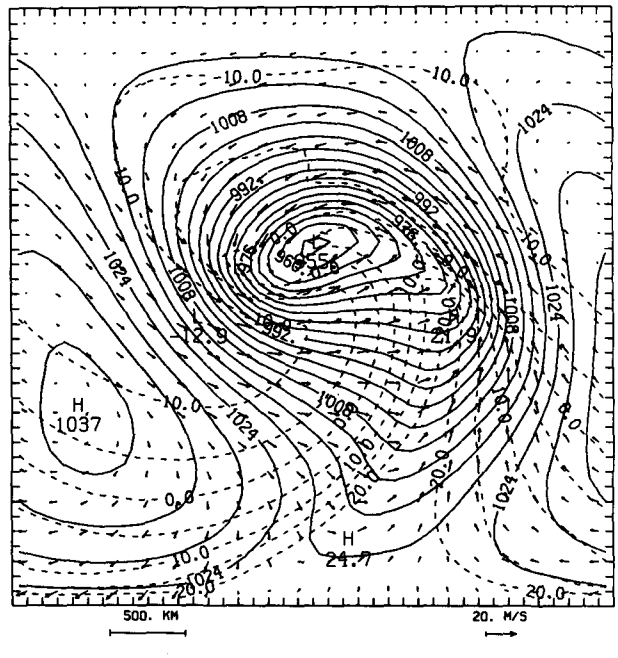


FIG. 19. Sea level pressure (solid), surface air temperature (dashed) and surface wind vectors for the no heat flux simulation at 36 h. Contours and labels as in Fig. 3.

shown in Fig. 20. The key difference is that in Exp. 3 the low-level thermal structure now resembles the sinusoidal SST distribution which results in temperature gradients less than those in Exp. 2 where there is no modification by surface heating. The phasing of the SST gradient with the location of low-level frontogenesis results in more pronounced warm and cold fronts. The most significant difference between this experiment and Exp. 2 is that changes above the boundary layer are not uniform in the vertical. Anticyclonic vorticity advection increases near the warm front at 850 mb which results in larger differential vorticity advection. Consistent with this stronger dynamical forcing are larger vertical velocities at the top of the boundary layer. A detailed analysis of the structural changes and effects of surface fluxes on the dynamics of the cyclogenesis is planned for a future paper.

Experiment 4, in which the latent heating is suppressed, indicates that the release of latent heat in the control simulation resulted in a slight increase in the rate of the development of the cyclone as shown in Fig. 7. As expected from the self-development concept, the 500 mb wave amplification was less than in the control. The effect was relatively small and latent heating in the control produced a cyclone that was only 5 mb deeper than in Exp. 4. The maximum diabatic heating rate of 5°C day$^{-1}$, computed as a residual of the heat budget averaged over a 2500 km × 2500 km region, occurred in the upper troposphere of the model cyclone. The maximum 500 mb temperature difference between the control and Exp. 4 was 5°C and occurred over the surface warm front, which confirms that diabatic heating produced these differences. The diabatic heating in the control experiment is far less than the 25°C day$^{-1}$ averaged over a 4° latitude region reported by Liou and Elsberry (1986) for an explosive cyclone in the western Pacific. The maximum 24 hour rainfall associated with the model storm was 2.99 cm, which occurred over a very small area. The relatively light rainfall and small heating rates are consistent with the minor impact of latent heat release in this simulation.

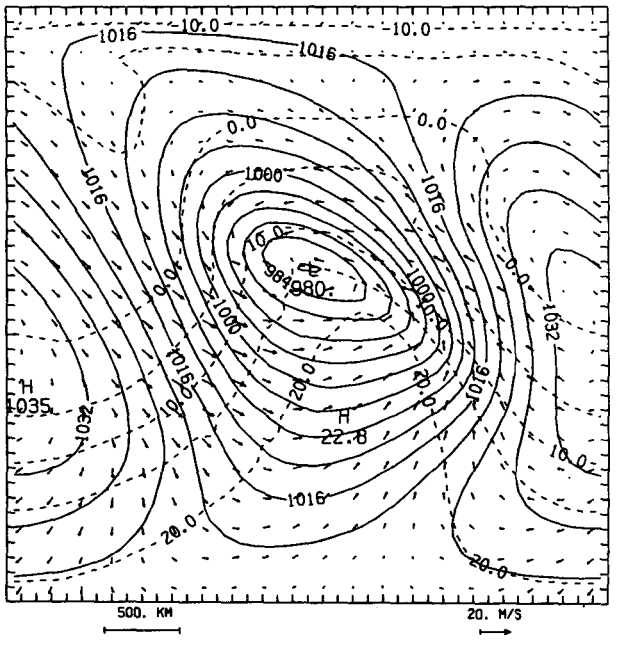


FIG. 20. Sea level pressure (solid), surface air temperature (dashed) and surface wind vectors for the sinusoidal SST simulation at 24 h. Contours and labels as inFig. 3.

### c. *Sensitivity to initial state*

As suggested by the previous model simulations, the development of the model cyclone occurs primarily as a result of the initial baroclinic instability. As originally found by Charney (1947) and Eady (1949) the cyclogenesis is sensitive to both the mean static stability and the mean meridional temperature gradient. However, the important question is how large these effects are compared to the influence of the physical factors during development. Reducing the low-level static stability of the initial state in Exp. 5 by as much as 50% for some regions in the warm sector and at least 30% elsewhere, increases the deepening rate of the model cyclone to 1.65 mb h$^{-1}$ and also produces a convective cloud band in the cold sector, which is occasionally observed in marine cyclones. The surface pressure, temperature and wind fields at 24 h (not shown) indicate a more intense cyclone than the control simulation. However, the PBL temperature structure is similar to that found in the control. The primary differences with the control experiment are larger 500 mb wave amplitude and vorticity (not shown). Vertical velocities at the top of the PBL (Fig. 21) exceed 1 m s$^{-1}$, which is more than twice that found in the control, consistent with stronger vorticity advection aloft. The associated PBL convergence substantially enhances the low-level vorticity. Another interesting feature is the development of a line of convection within the cold sector which was not observed in the control simulation and is shown (Fig. 22) in the cross section through the cold front along a line similar to line C–C in Fig. 8 for the control simulation. This convective feature was probably enhanced by upper-level positive vorticity advection west of the surface cyclone and the reduced static stability in the midtroposphere.

Increasing the static stability by as much as 15% in the low levels in Exp. 6 reduced the deepening rate to 1.2 mb h$^{-1}$. There were associated decreases in the upper-level wave amplitude and vorticity compared to the control experiment.

The magnitude of the initial baroclinity also has a profound influence on the deepening rate and resultant surface cyclone intensity as baroclinic instability theory predicts. The 27 h deepening rate is substantially reduced to 0.85 mb h$^{-1}$ (Fig. 7) by a relatively small (10°C) decrease in the meridional temperature gradient

in Exp. 7, although the maximum temperature gradient is nearly the same as in the control. Thus, the vertical wind shear is similar, although the jet core is much more narrow in this simulation. There is less amplification of the upper-level wave and consequently less vorticity advection aloft. From the self-development perspective, the initial thermal advection is less, which reduced the amplification of the 500 mb wave. In summary, the changes in the initial static stability and baroclinity had a greater effect on subsequent development than any of the physical factors that influenced the cyclone during development.

## 4. Discussion

These model simulations confirm that baroclinic instability in a channel-flow model with realistic physics is sufficient for rapid cyclogenesis and suggests which factors are most important. Key factors in baroclinic instability are the vertical wind shear and static stability, as shown originally by Charney (1947) and Eady (1949). The model physics and initial states used in this study are more complex than the linear theories of Eady (1949) or Charney (1947) but clearly demonstrate the dependence on these key factors. The important result from this study is that realistic choices of initial static stability and meridional temperature gradient with realistic model physics can yield explosive development rates over marine areas. Relatively small changes in the low-level static stability or meridional temperature gradient produced significant modifications to the deepening rates of the model cyclone. This confirms the previous results of Staley and Gall (1977) which indicate that low-level static stability changes have significant impact on the development rate of baroclinic waves. These results suggest that the effect of surface heat fluxes prior to development on static stability and the horizontal temperature gradient is important to the subsequent development, as previously suggested by Danard and Ellenton (1980).

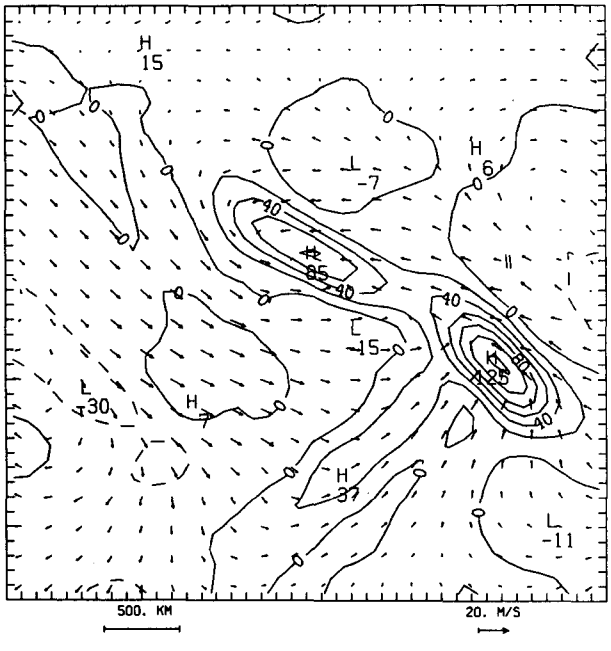


FIG. 21. Vertical velocity at the top of the PBL ($\sigma$ = 0.913) and surface wind vectors for the low static stability simulation at 24 h. Vertical velocity is in $10^{-3}$ m s$^{-1}$ with a 20 × $10^{-3}$ m s$^{-1}$ contour interval. Wind vectors as in Fig. 3.

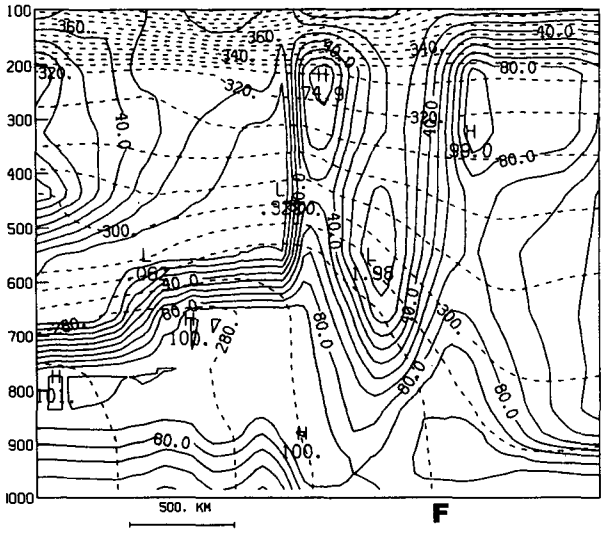


FIG. 22. Cross section of potential temperature (dashed) and relative humidity (solid) through cold front for the low static stability simulation at 24 h. Potential temperature is in °C with a 5° contour interval. Relative humidity is in % with a 10% contour interval. Vertical coordinate is pressure in mb. Horizontal length scale in km and cold front location (indicated by *F*) appear at the bottom.

Sensitivity to upper-level forcing by positive vorticity advection or divergence associated with a propagating jet streak was not tested, but differing amounts of upper-level forcing developed as a result of the differing initial baroclinity. From a self-development perspective, the rapid development of the model cyclone initially results from low-level thermal advection with little upper-level positive vorticity advection. As the upper-level wave amplifies, due primarily to the low-level thermal advection in the model cyclone, the upper-level vorticity advection increases. Enhanced upper-level forcing by a propagating jet streak as found for the Presidents' Day storm (Uccellini et al., 1984) and possibly the *QEII* storm (Uccellini, 1986) would certainly modify this self-development process. However, for the model cyclogenesis, the jet streak and tropopause fold develop as a result of the upper-level wave amplification and do not contribute independently to the cyclogenesis. The development of these upper-level features are a result of the baroclinic instability as previously demonstrated by Newton and Trevisan (1984), and cannot be readily separated from the other processes in the model cyclogenesis. The model results suggest that with stronger upper-level forcing the deep-

ening rate increases, particularly if the upper-level forcing is a result of baroclinic self-development.

Strong latent heat release in convection is not required for rapid development of this model cyclone, although the release of latent heat did contribute to a slightly increased rate of development. Previous studies by Tracton (1973) and Gall (1976) have established this effect of latent heating on cyclogenesis. The critical question revolves around the magnitude of the heating in explosive atmospheric cyclogenesis and whether it is due to convection. If a convective instability of the second kind (CISK) process is crucial to rapid development as hypothesized by Gyakum (1983b) for the *QEII* storm or Sardie and Warner (1983) for polar lows, then the heating rate will be significant. Liou and Elsberry (1987) found latent heating rates of 25°C day$^{-1}$ for the period of rapid development for a western Pacific cyclone. However, the model cyclone developed rapidly with a latent heating rate due to parameterized convection of only 20%, the value reported by Liou and Elsberry (1987), which suggests that strong diabatic heating is not essential in all rapidly developing cyclones.

The sea surface temperature distribution and associated air–sea interaction significantly modified the development of the model cyclone. When the surface heat and moisture fluxes tend to reduce the low-level baroclinity, the development rate of the model cyclone slows significantly. This damping effect has been previously identified by Mansfield (1974) for a linear baroclinic instability model and by Danard and Ellenton (1980) for several cases of east coast cyclogenesis. Results from this study indicate that this damping is confined to layers below 850 mb. Danard and Ellenton (1980) also found that the surface fluxes enhanced the development only during the initial stages when they reduced the low-level static stability and enhanced the initial baroclinity, which is reflected in the sensitivity of the model cyclogenesis to these factors in the initial conditions. Reed and Albright (1986) found this effect of stability modification to be important for an eastern Pacific cyclone. This study further suggests that when the SST distribution leads to a distribution of heat flux which is in phase with the low-level baroclinity and produces positive heat fluxes in the warm updraft region of the developing cyclone, the development may be enhanced substantially due to changes above the boundary layer. Both reduced midtropospheric static stability and increased latent heat release contribute to the increased development rate. Bosart (1981) identified this effect for the Presidents' Day storm where surface heat and moisture fluxes to the northeast of the cyclone center provided an important heat and moisture source for the developing cyclone. Additional evidence of phasing between the low-level baroclinity and the SST distribution is found in Sanders (1986), who shows a strong correspondence between the cyclone track for strong "bombs" and the Gulf Stream.

## 5. Summary and conclusions

Numerical simulations of cyclogenesis in a baroclinic channel-flow model with friction and heating have revealed that baroclinic instability is sufficient to yield explosive development and that the development rate is sensitive to a number of factors. The initial meridional temperature gradient and mean static stability have the greatest influence on the subsequent development as predicted by baroclinic instability theory. Relatively small changes of 10°C or 1°C km$^{-1}$ in these factors were sufficient to alter the development rate by 40% and 15% respectively. Other physical processes acting during the period of development can modify the baroclinic instability and associated self-development process by nearly as much as the initial state factors. Latent heating contributed to increasing the development rate by less than 10% and was not necessary to produce rapid development of the model cyclone. The effects of surface heat and moisture fluxes varied from reducing the development rate by as much as 25% to increasing the development rate by as much as 15%, depending upon the distribution of fluxes in the cyclone.

Modification of the development of the model cyclone by interaction with the sea surface depended upon the phase of the surface heat and moisture fluxes relative to the low-level temperature distribution. A surface flux distribution that reduces the low-level baroclinity damps the baroclinic instability by counteracting low-level thermal advection and reduces the deepening rate of the surface cyclone. A surface flux distribution that enhances the low-level baroclinity increases the development of the surface cyclone. A sea surface temperature distribution that is in phase with the low-level thermal wave in the atmosphere produces upward heat and moisture fluxes in the warm air sector of the cyclone, which resulted in greater precipitation and lower static stability above the boundary layer as well as a faster growth rate. This phasing between the sea surface temperature and thermal wave in the atmosphere suggests that during certain periods of the development, air–sea heat and moisture fluxes may significantly enhance the cyclogenesis by reinforcing the atmospheric baroclinity, reducing the midtropospheric static stability, and supplying additional moisture to the cyclone.

*Acknowledgments.* The authors would like to acknowledge the helpful advice and suggestions provided by Robert G. Fleagle, Richard J. Reed and Chester W. Newton. Critical review of an earlier version of this manuscript by Russell L. Elsberry is also gratefully acknowledged. The first author is thankful for the support provided by the Advanced Study Program at the National Center for Atmospheric Research while performing this research.

## REFERENCES


Agee, E. M., and F. E. Lomax, 1978: Structure of the mixed layer and inversion layer associated with patterns of MCC during AMTEX '75. *J. Atmos. Sci.*, **35,** 2281–2301.

Anthes, R. A., 1977: A cumulus parameterization scheme utilizing a one-dimensional cloud model. *Mon. Wea. Rev.*, **105,** 270–286.

——, and T. T. Warner, 1978: Development of hydrodynamic models suitable for air pollution and other mesometeorological studies. *Mon. Wea. Rev.*, **106,** 1045–1078.

Bosart, L. F., 1981: The Presidents' Day snowstorm of 18–19 February 1979: A subsynoptic scale event. *Mon. Wea. Rev.*, **109,** 1542–1566.

——, and S. C. Lin, 1984: A diagnostic analysis of the Presidents' Day storm of February 1979. *Mon. Wea. Rev.*, **112,** 2148–2177.

Brown, R. A., and W. T. Liu, 1982: An operational large-scale marine planetary boundary layer model. *J. Appl. Meteor.*, **21,** 261–269.

Buzzi, A., T. Nanni and M. Tagliazucca, 1977: Midtropospheric frontal zones: Numerical experiments with an isentropic coordinate primitive equation model. *Arch. Meteor. Geophys. Bioklim.*, **A26,** 155–178.

Charney, J. G., 1947: The dynamics of long waves in a baroclinic westerly current. *J. Meteor.*, **4,** 135–163.

Chen, T.-C., L.-B. Chang and D. J. Perkey, 1983: Numerical study of an AMTEX '75 oceanic cyclone. *Mon. Wea. Rev.*, **111,** 1818–1829.

Danard, M. B., and G. E. Ellenton, 1980: Physical influences on East Coast cyclogenesis. *Atmosphere: Atmos.–Ocean,* **18,** 65–82.

Eady, E. T., 1949: Long waves and cyclone waves. *Tellus,* **1,** 33–52.

Fritsch, J. M., E. L. Magaziner and C. F. Chappell, 1980: Analytic initialization for three-dimensional models. *J. Appl. Meteor.*, **19,** 809–818.

Gall, R. L., 1976: The effects of released latent heat in growing baroclinic waves. *J. Atmos. Sci.*, **33,** 1686–1701.

Gyakum, J. R., 1983a: On the evolution of the *QEII* storm. Part I: Synoptic aspects. *Mon. Wea. Rev.*, **111,** 1137–1155.

——, 1983b: On the evolution of the *QEII* storm. Part II: Dynamic and thermodynamic structure. *Mon. Wea. Rev.*, **111,** 1156–1173.

Kuo, H. L., 1974: Further studies of the parameterization of the influence of cumulus convection on large-scale flow. *J. Atmos. Sci.*, **31,** 1232–1240.

Kuo, Y.-H., and R. A. Anthes, 1984: Semiprognostic tests of Kuo-type cumulus parameterization schemes in an extratropical convective system. *Mon. Wea. Rev.*, **112,** 1498–1509.

Lau, N. C., 1978: On the three-dimensional structure of the observed transient eddy statistics of the Northern Hemisphere wintertime circulation. *J. Atmos. Sci.*, **35,** 1900–1923.

Lin, S. C., and P. J. Smith, 1982: The available energy budget of a severe storm-producing extratropical cyclone. *Mon. Wea. Rev.*, **110,** 521–533.

Liou, C.-S., and R. L. Elsberry, 1987: Heat budgets of analyses and forecasts of an explosively deepening maritime cyclone. *Mon. Wea. Rev.*, **115,** 1809–1824.

Mansfield, D. A., 1974: Polar lows: The development of baroclinic disturbances in cold air outbreaks. *Quart. J. Roy. Meteor. Soc.*, **100,** 541–554.

Mullen, S. L., 1979: An investigation of small synoptic cyclones in polar air streams. *Mon. Wea. Rev.*, **107,** 1636–1647.

Newton, C. W., and A. Trevisan, 1984: Clinogenesis and frontogenesis in jet-stream waves. Part II: Channel model numerical experiments. *J. Atmos. Sci.*, **41,** 2735–2755.

Nuss, W. A., 1986: The influence of surface heat and moisture fluxes on explosive marine cyclogenesis. Ph.D. dissertation, University of Washington, 181 pp.

Petterssen, S., and S. J. Smebye, 1971: On the development of extratropical cyclones. *Quart. J. Roy. Meteor. Soc.*, **97,** 457–482.

——, D. L. Bradbury and K. Pedersen, 1962: The Norwegian cyclone models in relation to heat and cold sources. *Geofys. Pub.*, **24,** 243–280.

Reed, R. J., and M. D. Albright, 1986: A case study of explosive cyclogenesis in the eastern Pacific. *Mon. Wea. Rev.*, **114,** 2297–2319.

Roebber, P. J., 1984: Statistical analysis and updated climatology of explosive cyclones. *Mon. Wea. Rev.*, **112,** 1577–1589.

Rogers, E., and L. F. Bosart, 1986: An investigation of explosively deepening oceanic cyclones. *Mon. Wea. Rev.*, **114,** 702–718.

Sanders, F., 1971: Analytic solutions of the nonlinear omega and vorticity equation for a structurally simple model of disturbances in the baroclinic westerlies. *Mon. Wea. Rev.*, **99,** 393–407.

——, 1986: Explosive cyclogenesis over the west central North Atlantic Ocean 1981–84. Part I: Composite structure and mean behavior. *Mon. Wea. Rev.*, **114,** 1781–1794.

——, and J. R. Gyakum, 1980: Synoptic–dynamic climatology of the "bomb." *Mon. Wea. Rev.*, **108,** 1589–1606.

Sardie, J. M., and T. T. Warner, 1983: On the mechanism for development of polar lows. *J. Atmos. Sci.*, **40,** 869–881.

Staley, D. O., and R. L. Gall, 1977: On the wavelength of maximum baroclinic instability. *J. Atmos. Sci.*, **34,** 1679–1688.

Sutcliffe, R. C., and A. G. Forsdyke, 1950: The theory and use of upper air thickness patterns in forecasting. *Quart. J. Roy. Meteor. Soc.*, **76,** 189–217.

Tracton, M. S., 1973: The role of cumulus convection in the development of extratropical cyclones. *Mon. Wea. Rev.*, **101,** 573–593.

Uccellini, L. W., 1986: The possible influence of upstream upper-level baroclinic processes on the development of the *QEII* storm. *Mon. Wea. Rev.*, **114,** 1019–1027

——, P. J. Kocin, R. A. Peterson, C. H. Wash and K. F. Brill, 1984: The Presidents' Day cyclone of 18–19 February 1979: Synoptic overview and analysis of the subtropical jet streak influencing the precyclogenetic period. *Mon. Wea. Rev.*, **112,** 31–55.

——, D. Keyser, K. F. Brill and C. H. Wash, 1985: The Presidents' Day cyclone of 18–19 February 1979: Influence of upstream trough amplification and associated tropopause folding on rapid cyclogenesis. *Mon. Wea. Rev.*, **113,** 962–988.

Zhang, D., and R. A. Anthes, 1982: A high resolution model of the planetary boundary layer. Sensitivity tests and comparisons with SESAME-79 data. *J. Appl. Meteor.*, **21,** 1594–1609.